Film drop production over a wide range of liquid conditions

Daniel B. Shaw
Department of Mechanical and Aerospace Engineering, Princeton University, Princeton, New Jersey 08540, USA

Luc Deike*
Department of Mechanical and Aerospace Engineering, Princeton University, Princeton, New Jersey 08540, USA
and High Meadows Environmental Institute, Princeton University, Princeton, New Jersey 08540, USA

(Received 22 May 2023; accepted 18 January 2024; published 26 March 2024)

Bursting bubbles at the ocean surface can produce liquid drops which transport material into the atmosphere, impacting global climate dynamics through radiative balance and cloud condensation nuclei. Film drops are one of two primary types of spray. We present an extensive experimental study on film drop production, for a wide range of physicochemical liquid conditions, salinity, temperature in saltwater, and small contamination by surfactant. We discuss how thinning and rupture models in the literature are able to describe the film thickness at bursting, bubble lifetime, and number of supermicron film drops emitted. Existing theories for the film drainage rate and number of film drops are shown to be robustly consistent with the experimental results, and we provide prefactors of the scaling equations to enable their implementation into sea spray emission functions. The bubble's lifetime remains poorly described by existing scalings. While significant scatter remains when considering the film thickness at bursting, existing theories describe reasonably well the mean values when varying viscosity, temperature or surfactant contamination. However, we show that varying salinity induces a shift in film thickness which cannot be explained by existing scaling theories.

DOI: 10.1103/PhysRevFluids.9.033602

I. INTRODUCTION

Bubbles bursting at the ocean's surface have been the focus of considerable research [1,2] due to their ability to transport material (liquid, salts, biological components, chemical contaminants, etc.) into the air [3] at rates high enough to contribute significantly to global climate dynamics through the production of sea spray aerosols (SSA) which can serve as cloud condensation nuclei in the atmosphere [4]. Additionally, radiative balance models are affected by the order of magnitude uncertainties in the amount of sea salt emitted from the ocean [5,6].

Bursting bubbles have been shown to have a significant impact on the spread of pollutants such as oil spills [7] or red-tide events [8], and they are capable of pathogen transport [9–11]. The spray created by bursting bubbles has been studied in a variety of contexts including industrial processes like beer foams [12] or sparking wine [13] as well as natural processes such as volcanic eruptions [14]. However, some aspects of surface bubble physics remain under active scrutiny [15]. For example, prior works studying the effect of various conditions—such as salinity—on the lifetime of surface bubbles present conflicting conclusions [9,16,17]. The role of temperature

*ldeike@princeton.edu

on SSA production also remains unclear in the literature as some studies show an increase in the number of spray drops with temperature [18–22], while others show a decrease [23–25].

There is a rich, decades-long history of fluid-dynamics research on the drops produced by bubbles bursting, which can be formed by two distinct mechanisms. Jet drops arise from the pinch-off of a Worthington jet [26] at the center of a bubble's cavity, and have been the subject of considerable research [27–32] including the effect of varying conditions (liquid viscosity, surface tension, density, etc.) [33,34]. Film drops are created by the fragmentation of the bubble's thin-film liquid cap as described in Refs. [9,35]. Recent work has proposed a flapping film mechanism to explain the production of submicron aerosols [36] previously reported in the oceanographic community [1,37]. Simple questions about how film drops could change in various water quality conditions—temperature and biological activity—motivate a study of their production (characterizing film thickness at burst and bubble lifetime) [9] across a wide range of conditions.

We present an extensive experimental study on how changes in temperature, salinity, viscosity, and surfactant (weakly contaminating otherwise pure water) affects the production of film drops across a large range of bubble sizes. We directly image and analyze the creation of film drops with high-speed videos over a wide range of liquid conditions; present and experimentally test important equations for the lifetime, film thickness at burst, and drop number. We discuss extensively the applicability of scaling relationships presented in Refs. [9,35] derived for film thickness at bursting, bubble life time and bubble number, when varying systematically the liquid conditions, i.e., liquid viscosity, temperature, contamination by surfactant and salinity; some of which had not been tested experimentally. When the theoretical scaling hold, we provide prefactors to the model equations that can be used within sea spray emission functions modeling the number and size of drops produced by bursting bubbles for various physicochemical parameters (e.g., Refs. [3,38]).

The experimental methods and setup are first presented in Sec. II. After outlining the general physical parameters affecting film drainage in Sec. III, a formal model for cap drainage that accounts for both capillary pressure drainage as well as Marangoni stress's affect on marginal regeneration is presented in Sec. IV. Results and a theoretical model for the average bubble lifetime and film thickness at burst are presented in Sec. V. Both Secs. IV and V build upon previously proposed models and discuss their ability to accurately describe bubble cap drainage across a wide range of conditions. Of note is the estimate of the film thickness at burst which is a critical variable of global climate models which provides much-needed data for this model across many conditions. The film drop formation physics and existence in various conditions are described in Sec. VI, which formalizes the regimes under which drops can be created and presents results across all conditions. Finally, the number of film drops produced per bubble is shown in Sec. VII to be a function of geometric parameters. Care is taken to report all dimensionless prefactors to facilitate use of the equations into any modeling applications.

II. EXPERIMENTAL METHODS

To study the affect of varied liquid conditions on the production of film drops, air bubbles of various sizes are created in a liquid bath of different conditions as outlined in Appendix Table I. Five groups of trials are performed, with each dataset varying a single liquid parameter over a sweep of bubble size at each condition; the parameters being surfactant contamination, viscosity in water-glycerol mixture, synthetic seawater at various temperatures, and synthetic seawater at various salinities. This work varied liquid composition and did not investigate the effect of air contamination.

The role of surfactant contamination is considered in two of the datasets; one contained sodium dodecyl-sulfate, SDS, (with a maximum concentration of 150 μmol), and the other contained Triton X-100, TX100, (with a maximum concentration of 10 μmol) both added to de-ionized water (DI water). The SDS is from Fisher Scientific and with a purity of $\geqslant$99%. The TX100 (MQ100 Quality Level) was purchased from Millipore Corporation. The CMC, critical micelle concentration, of each is 8200 μmol and 220 μmol, respectively, which are both more than an order of magnitude higher

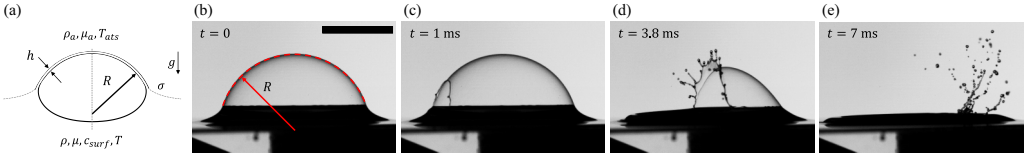

FIG. 1. (a) The geometry of a surface bubble and relevant physical parameters are shown. The thin-film liquid cap has a thickness h and radius R. The density, viscosity, and temperature of the liquid is ρ, μ, and T, respectively. In the air phase above the bubble, they are ρ_a, μ_a, and T_{ats}, respectively. The surface tension of the liquid-air interface is denoted by σ, and the concentration of surface-active molecules, surfactants, is c_{surf}. (b) Example of a $R = 10$ mm bubble (the black bar is also 10 mm long) in DI water with $c_{\text{surf}} = 8\,\mu$mol of Triton X-100 producing ≈80 drops as it bursts. From the moment a bubble created underwater arrives at the liquid-gas surface (driven upwards by buoyancy) its thin-film liquid cap starts draining. At some point, a hole will nucleate in the cap and expand (c). As the thin-film retracts, its rim destabilizes to form ligaments (d) which pinch off to form drops (e).

than the maximum concentrations studied. Bubbles created in this regime of "weak" contamination have lifetimes between the regimes of immediate bursting for pure DI water bubbles and saturated soap bubbles which can last for minutes or hours. The level of contamination within this range has been previously shown to affect the rate at which collections of surface bubbles can merge and burst [39]. This regime of weak contamination overlaps with the experimental parameters of a previous study which analyzed film drops created in tap water [35], and this work aims to explore more controlled contaminations and variety of liquid conditions.

The role of viscosity is examined in two other datasets. In one, glycerol was added at three different ratios with DI water (10%, 20%, and 30% by mass); varying the viscosity by a factor of three from that of pure DI water. As the density and surface tension of these mixtures change less than 2%, this dataset tests the effect of altered viscosity. In another one, we employed synthetic seawater (35 g/kg) at temperatures ranging from 1.2 to 35 °C. This dataset explores the role of temperature either as a direct variable influencing bursting or as a parameter varying viscosity. Another dataset featured synthetic seawater of salinity 17.5 and 35 g/kg (i.e., typical seawater salinity and 1/2 of seawater salinity), which reveals subtle effects of salt concentration on lifetime and film thickness. The synthetic seawater was purchased from Ricca Chemical Company (ASTM D 1141 Substitute Ocean Water without Heavy Metals) and Lake Products Company LLC (Sea-Salt ASTM D1141-98) which produces substitute seawater with primary salts of: NaCl (24.53 g/l), $MgCl^2$ (5.20 g/l), Na^2SO^4 (4.09 g/l), $CaCl^2$ (1.16 g/l), and KCl (0.695 g/l).

The size of a surface bubble is described in this work by the radius of curvature of the thin-film liquid cap, R, as shown in Fig. 1(a). The bubbles ranged in size from $R = 1.5$ mm to $R = 15$ mm. An alternative metric of surface bubble size is the volumetric radius (R_{vol}) which is commonly defined as the radius that a sphere containing the same volume of air as the surface bubble would have. By solving the static Young-Laplace equation balancing surface tension and hydrostatic pressure, the equilibrium shape of surface bubbles can be determined numerically [40–42]. This is used to determine the relationship between R and R_{vol}, which is described and shown in Appendix B. The size of a surface bubble can also be described by the dimensionless Bond number [40], $\text{Bo} = \Delta\rho g R_{\text{vol}}^2/\sigma = R_{\text{vol}}^2/l_c^2$, where $\Delta\rho$ is the density difference between the liquid and gas, g is gravitational acceleration, σ is the liquid-gas surface tension, and l_c is the capillary length ($l_c = \sqrt{\sigma/\Delta\rho g}$). Bubbles of $\text{Bo} \ll 1$ reside almost entirely beneath the surface, and are nearly spherical while $\text{Bo} \gg 1$ bubbles are above the surface with a half-spherical cap.

Two high speed cameras are used to capture the relevant features of a bubble's life and bursting. A Phantom V2012 recording at 50 000 frames per second was used to record the bubble bursting and film drop creation process, and a Phantom 4K recording at 500 frames per second recorded the how long the bubble lasted on the surface before bursting. Different lenses and magnifications were

used for the various different bubble sizes. For the smallest bubbles of $R = 1.5$ mm, the maximum resolution is 8 μm/pixel, and the depth of field at this magnification was approximately 1.5 mm with a K2 DistaMax lens from Infinity Photo-Optical Company. Care was taken to only record bubbles for which the film drops can be clearly observed. In this manner, we estimate that the effective drop size able to be detected is a half-pixel (4 μm); as drops travel, it is possible to observe and count drops slightly less than one pixel in diameter because their track is apparent even though their size cannot be measured. The film drops produced are manually counted and each frame of the video is analyzed since no single frame of the video shows all of the drops produced due to the relatively small depth of field. Bubbles larger than $R \approx 5$ mm were imaged on a setup with resolution about twice as large as the spray drops measured and a depth of field $\geqslant$5 cm, so in many cases a single frame was able to capture all of the drops.

An example video sequence of an $R = 10$ mm bubble bursting in an 8 μ M solution of Triton X-100 surfactant at 22 °C is shown in Figs. 1(b)–1(e). From the moment a bubble created underwater arrives at the liquid-gas surface (driven upwards by buoyancy) its thin-film liquid cap starts draining. At some point, a hole will nucleate in the cap and expand [Fig. 1(b)]. As the thin-film retracts, its rim destabilizes due to centripetal destabilization to form ligaments [Figs. 1(c) and 1(d)] which pinch off to form drops [Fig. 1(e)]. This study does not observe the production of film drops via the flapping mechanism [36] (proposed to explain the production of submicron drops) for the range of bubble sizes and liquid conditions studied.

The bubble's cap radius is measured just prior to bursting as shown in Figs. 1(a) and 1(b). The cap's thickness is determined by measuring its retraction velocity which is observed to be the constant Taylor-Culick velocity: $V = \sqrt{2\sigma/(\rho h)}$ (where ρ is the density of the liquid and h is the film thickness), consistent with previous observations [35]. These measurements of the retraction speed provide a measure of the film thickness since the liquid properties are known. Approximately 2500 bubble bursting events like the one shown in Fig. 1 are measured, and about 55 000 film drops are counted.

Bubbles of various sizes are produced by varying the needle size through which air is pushed by a syringe pump (SyringePump NE-1000) very slowly so that only one bubble is produced at a time. All experiments except those which varied temperature were performed in a square petri dish 10 cm square by 3 cm tall, and the bubbles were created ≈2 cm below the free surface. For the trials with varied temperature, a different container sized 10 cm×10 cm×10 cm contained the liquid in which the bubbles were produced; the needles remained ≈2 cm below the free surface. To control the temperature, this container was placed into a temperature controlled bath with minimal surface area of the bath uncovered.

III. FILM THICKNESS FOR VARIOUS LIQUID CONDITIONS

The film thickness of the bubble cap, h, for each bubble in this study is shown in Fig. 2, as a function of the cap radius, R. The size of each marker indicates that bubble's lifetime. Various liquid conditions are explored, with varying surfactant contamination [Fig. 2(a)] and temperature in seawater [Fig. 2(b)]. A probability density function of the film thickness for various temperatures (for 3 mm $< R <$ 6 mm in size) is shown in Fig. 2(c). Film thicknesses for glycerol-water mixtures with varying viscosity are shown in Fig. 2(d) and salinity variations in Fig. 2(e) with the probability density functions of varied salinity presented in Fig. 2(f).

Across all of the conditions, some trends are clear. Longer lifetimes generally correspond with a thinner cap as the bubble has more time to drain. For a given bubble size and liquid condition, there is a considerable range (approximately one order of magnitude) of scatter in the film thickness across all of the data sets. A general trend that h increases with R can also be observed, but the relationship is nontrivial since h is strongly affected by the bubble's lifetime which can itself be a function of bubble size and liquid condition. There are also numerous complexities in the relationship between film thickness and the various controlling parameters, which can be seen by inspection of each condition.

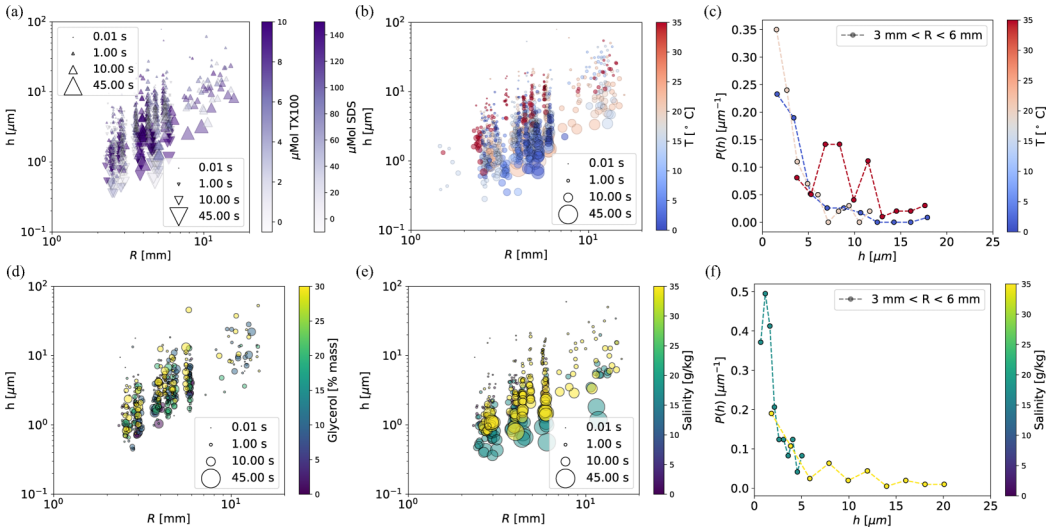

FIG. 2. The film thickness at burst, h, cap radius, R, and lifetime (marker size) are shown for every bubble measured in this study. The basic physics of cap film drainage across various datasets can be seen. For a given bubble size, longer lifetimes create a thinner cap film, although even at consistent bubble size and liquid condition there is a wide distribution of lifetimes and final cap thickness. Additionally, smaller bubbles generally produce thinner films for a given environmental condition. The relationship between film thickness and environmental condition however is nontrival since the lifetime of the bubble is affected by the liquid conditions and bubble size. Panel (a) shows variations in SDS (point down triangle) and Trixon X-100 (point up triangle) concentration. (b) Variations in liquid temperature for synthetic seawater: colder temperature leads generally to smaller films. (c) Histogram of the film thickness for 3 mm $< R <$ 6 mm for the bubbles at temperatures of 1.5 °C, 20 °C, and 35 °C. (d) Glycerol-water ratio. (e) Changes in salinity: thinner bubbles are observed for smaller salinity. (f) Histogram of the film thickness for 3 mm $< R <$ 6 mm for salinities of 17.5 and 35 g/kg.

Across variations of SDS and Triton X-100 concentration, Fig. 2(a), there is no clear trend between the thinnest films at each bubble size and surfactant concentrations; both the lifetime and drainage rate have been shown to be functions of surfactant concentration [39,43–45].

Figure 2(b) shows the same measurement but now as a function of the temperature of saltwater (for typical oceanic salt concentration). Colder liquids lead overall to thinner film thickness at burst with the data at 35 °C having a thicker cap at burst than the colder temperatures. A histogram of this data for 3 mm $< R <$ 6 mm at 1.5 °C, 20 °C, and 35 °C is shown in Fig. 2(c), and confirm the trends visible in B. Figure 2(b) shows that lifetime is not the only relevant parameter for determining the film thickness; it also increases with temperature. Coherent with previous findings [9], while increasing temperature decreases the liquid viscosity—which would increase the rate of viscous drainage—temperature gradients (which produce surface tension gradients) across the bubble's surface can alter drainage dynamics through Marangoni effects of marginal regeneration at the bubble's foot [46]. Varying concentrations of glycerol are shown in Fig. 2(d). Unlike decreasing temperature, increasing the viscosity of the liquid with glycerol produces thicker films: an effect expected by classic viscous film drainage theory [43,47,48], as already discussed by Ref. [9]. Finally, Fig. 2(e) shows that changes in liquid salinity affect both the lifetime and final film thickness with thinner films appearing for lower salinity concentration, an observation not explained by either viscous drainage or Marangoni stress. The histogram shown in Fig. 2(f) for the two salinities tested confirm this trend.

IV. BUBBLE CAP DRAINAGE

The drainage of a bubble's thin-film liquid cap is thought to be primarily controlled by three mechanisms: capillary pressure driving fluid out of the thin-film cap, viscous drag at the foot of the bubble in a pinched region, and marginal regeneration [9,35] (which can be influenced by Marangoni stress between the bubble's cap and the surrounding liquid).

Evaporation has been shown to play a role in bubble drainage dynamics and must be included in a complete model of film drainage dynamics [50]. Note that for bubble in an oceanlike environment, evaporation has been discussed as being important mostly for long-lived bubbles (lifetimes greater than O(20s) [51]), which only account for about 2% of bubbles in this study.

The primary force draining the bubble cap is capillary pressure. As surface bubbles have a hemispherical thin-film liquid cap, the pressure inside the cap is $2\sigma/R$ higher than that of the flat air-water interface next to the bubble. This pressure difference driving liquid out of the thin-film cap into to the surrounding liquid bath is determined purely by the surface bubble's geometry and the approximately constant surface tension of the liquid in the cap. Gravity can also contribute to a bubble's cap drainage [48], but has been shown to only be relevant for large bubbles of $R \geqslant 5l_c$ in the conditions of this study [35].

One of the forces resisting drainage of the cap is viscous drag from the liquid-gas interfaces. Surfactants, even in concentrations well below the CMC, are able to exert surface forces and rigidify interfaces [43], which enables the formation of a "pinched" region near the foot of the bubble where the cap joins the meniscus of the liquid bath [52]. This pinched region has long been observed in both surfactant-saturated soap films and much more dilute surfactant concentrations [53,54]. In the case of surface bubbles, a pinched region of size L and thickness δ is where the viscous drag on the draining liquid is assumed to be concentrated [35]. Balancing capillary pressure driving drainage with viscous drag over this region, a scaling is given by the Stokes equation:

$$\mu \frac{u_{\Delta P}}{\delta^2} \sim \frac{\sigma}{RL}. \tag{1}$$

Lhuissier and Villermaux [35] proposed that δ scales with h while L is set by matching the curvature of the rest of the bubble cap (maintaining capillary pressure), $1/R \sim h/L^2$, and find [35]

$$u_{\Delta P} = -c_1 \frac{\sigma}{\mu}\left(\frac{h}{R}\right)^{3/2}, \tag{2}$$

where the scaling prefactor c_1 is dimensionless.

Employing mass conservation ($\frac{dh}{dt} = \frac{uh\mathcal{P}}{S}$ where $\mathcal{P}$ refers to the perimeter at the foot of the bubble, S to the surface area of the cap, and $\mathcal{P}/S = \cot(\theta_c/2)/R \approx 4\sqrt{3}l_c/R^2$ [35] where θ_c is the angle subtended by the bubble's cap from the center of the cap to the meniscus) and integrating Eq. (2) provides an expression for how h changes in time [9,35]:

$$h/l_c = (6\sqrt{3}c_1)^{-2/3}\left(\frac{\mu l_c}{\sigma t}\right)^{2/3}\left(\frac{R}{l_c}\right)^{7/3}. \tag{3}$$

While we do not track the time evolution of the film thickness, we can evaluate Eq. (3) by considering the lifetime at burst, t, and the corresponding film thickness. Figure 3(a) plots the same data of water-glycerol mixture bubble drainage from Fig. 2(d), as a function of Eq. (3). The collapse of the data shows that Eq. (3) adequately describes the viscous aspect of cap drainage for water-glycerol mixtures. A similar collapse of the data to Eq. (3) can be seen for the varied data at varied salinity from Fig. 2(e) in Fig. 3(b).

Equations (2) and (3) do not however describe the effect of varied temperature in seawater as shown in Fig. 3(b). The data is more scattered and clearly banded by temperature over the entire dataset with Eq. (3) overestimating the film thickness of cold saltwater by almost an order of magnitude; while the colder water has a higher viscosity, it drains faster. This inconsistency

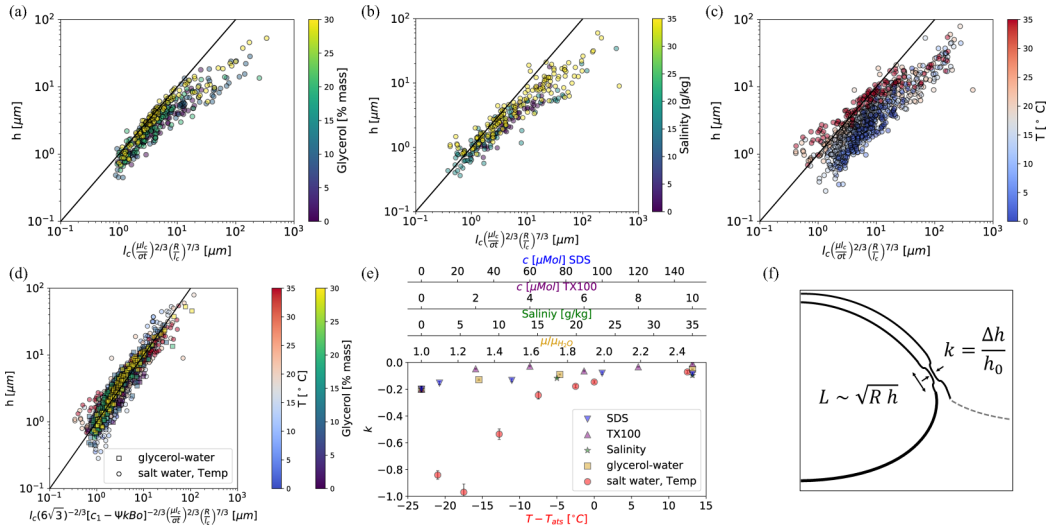

FIG. 3. Film cap drainage data compared to models. (a) The film thickness at burst of our 521 glycerol-DI water bubbles [the same data points shown in Fig. 2(d)] are presented and compared to Eq. (3) which assumes that the capillary pressure driving fluid out of the thin-film cap is resisted by viscous stress across the foot of the bubble alone. Increasing the glycerol content of the mixture increases the viscosity (by a maximum factor of 2.5 in this work), and the data collapses well to the model. (b) Similar plot with two salinity concentrations. Again, the drainage model Eq. (3) represents well the data. (c) Similar plot for increasing seawater temperature. Film thickness is significantly reduced when colder temperature are considered, and the overall spread of the data is much larger than in A and B. Increasing the temperature of saltwater increases its viscosity, but Eq. (3) does not describe the film thickness of our 903 bubbles at various temperatures (1.2 to 35 °C). It overestimates the film thickness of the coldest bubbles by almost an order of magnitude. (d) A model which explains the drainage of bubbles both the glycerol and saltwater with varied temperature is developed by assuming that it is a function of both viscous drainage and marginal regeneration [9]. Both datasets collapse to the model [Eq. (5)], where $c_1 = 0.1$—which is the same order of magnitude of $c_1 = 1/3$ found in other work [9]—and $\Psi = O(0.5)$ is estimated from results of prior studies that $k \approx 0.2$ at room temperature [35,49]. The values of k in Eq. (5) are obtained by least square fit for each liquid condition. (e) The varied liquid conditions are shown to alter k which is estimated by fitting the data at each condition to Eq. (5). Empirically determined values of k are shown for all conditions tested. Variations in SDS and TX100 concentration are shown in the blue point-down and purple point-up triangles, respectively. Variations in salinity are presented as green stars, changes in glycerol content are gold squares, and different temperatures are shown as red circles. Across all conditions, the only one for which a significant variation in the drainage rate is observed is temperature variation, which is shown by the range of $-0.9 < k < -0.1$. For all other liquid conditions, $-0.2 < k < 0$ which indicates that $u_{\Delta P}$ dominates the film cap's drainage rate. (f) The geometry of the bubble's foot (half of the bubble is shown) which is highlighted by a pinched region, defining the parameters considered in the model proposed by Refs. [9,35].

prompts the consideration of another process affecting the cap's drainage: the plumes rising out of the bubble's foot.

Because the bubble's foot is thinner than the rest of the cap, convectionlike plumes (named marginal regeneration) rise from this region into the bubble's cap. Observed in soap films at Plateau borders [46,53,55] as well as bubbles [9,35,50,56], they rise due to their apparent buoyancy to replace thicker film in the bubble's cap in a *sliding puzzle dynamics* manner [54,57]. The buoyancy force acting on a patch of film (of height $= L$, width λ, and thickness of $h_0 + \Delta h$ where h_0 is the thickness of the surrounding film) at the bubble's foot is $F_B \sim \rho g \Delta h L \lambda$, and the drag force is $F_D \sim \mu \lambda u_{\Delta\sigma}$ where $u_{\Delta\sigma}$ is the velocity of the patch. Balancing buoyancy and drag provides an

estimate of the plume rise velocity [9]:

$$u_{\Delta\sigma} = \Psi k \mathrm{Bo} \frac{\sigma}{\mu} \left(\frac{h}{R} \right)^{3/2}, \tag{4}$$

where $k = \frac{\Delta h}{h_0}$ [see the inset of Fig. 3(d)] and Ψ is a dimensionless prefactor. Assuming that the bubble cap's drainage is a function of both viscous drag in the foot and marginal regeneration, the total velocity of fluid draining is $u = u_{\Delta P} + u_{\Delta\sigma}$ which is integrated as discussed by Poulain *et al.* [9] to

$$\frac{h}{l_c} = (6\sqrt{3})^{-2/3} [c_1 - \Psi k \mathrm{Bo}]^{-2/3} \left(\frac{\mu l_c}{\sigma t} \right)^{2/3} \left(\frac{R}{l_c} \right)^{7/3}. \tag{5}$$

As temperature affects surface tension as well as viscosity, it can alter the marginal regeneration rate. The cap is exposed to the ambient air and can have a different temperature (and surface tension) relative to the liquid bath, creating a surface tension gradient (or Marangoni stress) over the bubble's foot. When the cap is warmer than the liquid bath (as is the case when the liquid bath is colder than the surrounding air), its surface tension is smaller than that in the bulk. This Marangoni stress alters the drainage rate by changing k and the bubble's ability to form thin plumes to rise through the cap. One important note is that because marginal regeneration is always distributing patches of thin-film from the pinched region into the cap by buoyancy, the pinched region is thinner than the cap above it: $k < 0$.

Figure 3(c) shows how the drainage of bubbles in glycerol and saltwater with varied temperature collapse together to Eq. (5). We find $c_1 \approx 0.1$ which is the same order of magnitude of $c_1 = 1/3$ found in other work [35]. As prior studies estimate that $k \approx 0.2$ at room temperature [35,49], Ψ is estimated to be $\Psi = O(0.5)$ to align with those results. We then determine k by least-square fitting each liquid condition. Empirically determined values of k are shown in Fig. 3(d) with the glycerol-water mixture data as square symbols (x axis at the top of the plot) and the saltwater with varied temperature data as circles (x axis at the bottom of the plot). Hence, the Marangoni correction provides a path to collapse all data onto a single curve with limited remaining scatter around Eq. (5).

However, the parameter k is determined empirically and there is no predicting theory at this point to explain its variations with various physicochemical parameters. The small range of $|k| < 0.2$ for glycerol is only a small correction, which is expected as viscous drainage dominates. The salinity dataset also finds $|k| < 0.2$, but we caution again that variations in salinity show a larger scatter than the other datasets, suggesting an effect of salt concentration not described by the above formula. For variations in SDS and Triton X-100 concentration studied, k is also shown to have a small range of $|k| < 0.2$.

In contrast, k ranges by almost an order of magnitude from about -0.9 to -0.1 for the saltwater at 5 °C to 35 °C, respectively, coherent with the fact that large temperature gradients will enhance surface tension gradients at the film interface and enhance Marangoni stresses. As outlined in Ref. [9], a temperature difference across the foot of the bubble produces a Marangoni stress there which can serve to thicken or thin the foot. The reported values of k serve as an indirect measure of this thickness change. The ambient temperature for all of the trials was approximately 22.5 °C, and the largest magnitude of k is when $T = 5$ °C and the liquid temperature is well below that of the ambient air.

V. AVERAGE CAP THICKNESS AND LIFETIME

While Eq. (5) describes the cap's drainage rate, it does not provide prediction about the average cap thickness of a bubble when it bursts for a given size and environmental condition, $\langle h \rangle$; it requires knowledge of the average lifetime of a bubble, $\langle t \rangle$, which is itself a function of bubble size and environmental conditions. Poulain *et al.* [9] hypothesized that a film will burst if a patch of surface contaminant is transported across the film in less time than it disperses. A contaminant of size δ_c was

assumed to be mixed by a velocity boundary layer (scaling as $\delta_u \sim \nu/u$) in a laminar fashion from a rigid surface: $\delta_c \sim \delta_u \mathrm{Sc}^{-1/3}$. Sc is the Schmidt number defined as $\mathrm{Sc} = \mu/\rho D$ (D is the molecular diffusion of the contaminant) and physically describes how quickly the contaminant disperses by shear-enhanced mixing versus diffusion. Employing the Einstein relation for molecular diffusion of spherical particles of radius r—estimated to be $O(10^{-9}$ m) in this study—$D = \frac{k_B T}{6\pi\mu r}$. As such, an estimate of Sc is

$$\mathrm{Sc} = \frac{6\pi r \mu^2}{\rho k_B T}. \tag{6}$$

Note, the estimate of constant contaminant size $r \approx O(10^{-9}$ m) across various conditions is a hypothesis open to revision in future work. This assumption could be changed for instances of surfactant micelles, nondissolved contaminants such as micro- or nanoscale plastic pollution, or solid salt crystals.

As such, the timescale of transport across the film becomes $\tau_{\mathrm{trans}} \sim h\delta_u \mathrm{Sc}^{-1/3}/D$, and the film is assumed to rupture when τ_{trans} is less than the residence time of the contaminant ($\tau_{\mathrm{res}} = R^2/u l_c$), leading to an average film thickness,

$$\langle h \rangle = c_h \frac{R^2}{\mathrm{Sc}^{2/3} l_c}, \tag{7}$$

where c_h is a nondimensional prefactor. Setting $h = \langle h \rangle$ in Eq. (5) also leads to an equation for $\langle t \rangle$:

$$\langle t \rangle = c_t (6\sqrt{3})^{-1} [c_1 - \Psi k \mathrm{Bo}]^{-1} \frac{\mu l_c}{\sigma} \mathrm{Sc} \left(\frac{R}{l_c} \right)^{1/2}, \tag{8}$$

where c_t is a nondimensional prefactor.

The average cap thickness, $\langle h \rangle$, in Eq. (7) is compared to that of seawater with varied temperature in Fig. 4(a) and that of glycerol-water mixtures in Fig. 4(b). The semitransparent circles are the raw data, while the solid squares are averages of the raw data for a given bubble size and temperature, with the error bars corresponding to one standard deviation. The black line has a slope of 1 with $c_h = 0.04$ for both environmental conditions. Reasonable agreement between the data and the model Eq. (7) is observed, with less than an order of magnitude in data scatter. The other environmental conditions show a similar scatter for all cases, with the salinity variations showing the largest spread.

While the data shows good agreement with Eqs. (5) and (7) for the film thickness, it does not agree well with Eq. (8) for the average lifetime for all of the environmental conditions, even though Eq. (8) is simply the combination of Eqs. (5) and (7) (setting $h = \langle h \rangle$). Figures 4(c) and 4(d) show the results for bubble lifetime compared to Eq. (8) for saltwater at various temperatures and glycerol-water mixtures, respectively. The hollow circles show all recorded lifetimes while the solid squares show the average values for a given size and environmental condition. The saltwater at various temperatures does not show a clear match to the trend line, particularly at larger values of the x axis. The solid line indicates the theoretical prediction and does not describe the data over the range of parameters tested. The results for various glycerol-water mixtures aligns better with Eq. (8). Both the trend lines shown in Figs. 4(c) and 4(d) have prefactors of $c_t = 20$. Unlike measurements of $\langle h \rangle$, the scatter of the data is large compared to the effect of varying liquid conditions. The expected bubble lifetime of every dataset is consistent with these observations, and the significant scatter makes it difficult to clearly conclude on the bubble lifetime for the presented range of conditions. The distribution of bubble lifetimes has been previous reported [35], and we find similar ranges compared to the average values.

Prior studies have come to conflicting conclusions for the effects of different conditions [9] on a bubble's lifetime. Equation (5) matches the measured film thickness so well as shown in Fig. 3(c) because it uses the measured lifetime of each bubble. As long as Eq. (5) describes an accurate drainage rate, variations in an individual bubble's lifetime do not affect its agreement with Eq. (5); the change in both lifetime and film thickness are captured according, and the spread of each

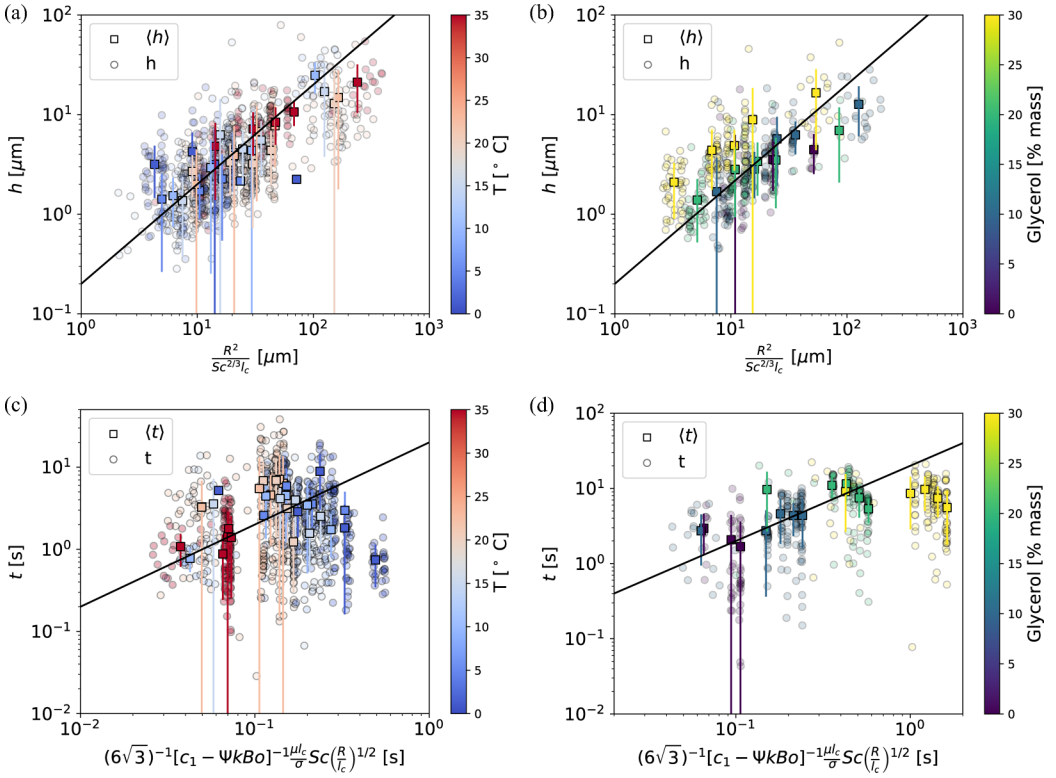

FIG. 4. (a), (b) The cap thickness at burst h, and its ensemble average $\langle h \rangle$, for saltwater at various temperatures (a) and glycerol content (b). Empty circles are h for each realization while $\langle h \rangle$, is bin averaged for given bubble size and environmental condition (here temperature). The data collapses to Eq. (7) with $c_h = 0.02$ for both graphs. (c), (d) The expected lifetime of bubbles in saltwater at various temperatures (c) and glycerol content (d) is compared to Eq. (8) with $c_t = 20$ in both. Individual bubble lifetimes t are shown as empty circles while ensemble averages $\langle t \rangle$ are solid squares. We do not observe a clear collapse of the data to Eq. (8) across different temperatures, but the data collapses reasonably well for the various glycerol mixtures. At every bubble size and environmental condition, there is about an order of magnitude spread of the measured lifetimes.

measurement is not described. In contrast, the measured film thickness and lifetime of bubbles at each condition are widely scattered as shown in Figs. 4(a) and 4(b). Note, since Sc is here assumed independent of surfactant concentration, the bubble radius R, is the only parameter to vary significantly in Eqs. (7) and (8) for surfactant concentration variations.

VI. DROP FORMATION AND EXISTENCE

We now analyze drop production by a bubble's liquid thin-film retracting in a centrifugal manner. As has been described in prior work [35], the film retracts at the Taylor-Culick velocity, forming a fluid rim at its edge which follows the shape of the bubble's cap: an arc of radius R. As such, the rim undergoes a centripetal acceleration of $a = V^2/R \sim \sigma/(\rho h R)$ to destabilize in a Rayleigh-Taylor fashion with a wavelength of $\lambda = \sqrt{Rh}$ and timescale of $\tau = [\sigma/(\rho a^3)]^{1/4} \sim \sqrt{\rho (Rh)^{3/2}/\sigma}$ [35].

One fundamental question of film drop production is if drops will be formed at all. The existence of film drops is measured for all conditions, and the results for bubbles in saltwater of varying size and temperatures is shown in Figs. 5(a). Figure 5(b) shows the same information for glycerol-water mixtures. Each point represents an individual bubble burst; circles indicate that no film drops were

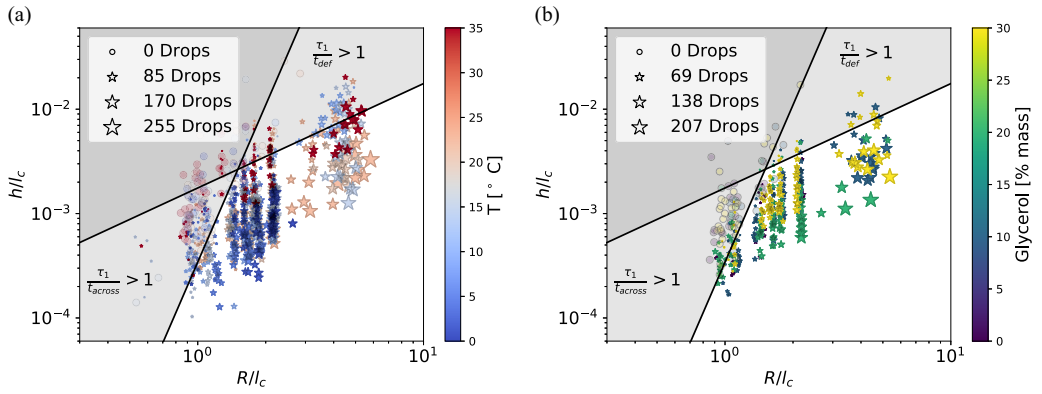

FIG. 5. Phase portraits of where film drops are formed for a given bubble size and film thickness. (a) shows the results for for saltwater at various temperatures, and (b) shows the existence phase portrait for various glycerol-water mixtures. There are multiple ways in which film drops may not be produced; the film may deflate ($t_{\rm def}$) or the rim can reach the opposite side ($t_{\rm across}$) before the cap has time to form a drop (τ_1). The scalings for $\tau_1/t_{\rm def} > 1$ and $\tau_1/t_{\rm across} > 1$ are shown by the gray regions without any fitting parameters. The circular points mark where no drops were produced while the stars correspond to bubbles that produced drops with the size of the star indicating how many film drops were produced. The scalings provide a good measure of the phase space where drops can be formed.

produced while stars indicate film drops were formed with the marker sizes representing the number (ranging from 1 to 255). The data is plotted as a function of film thickness and cap radius, both normalized by the capillary length.

There are two primary conditions in which film drops are not produced. First, a film can retract to the edge of the bubble—in a timescale $t_{\rm across}$—faster than the first drop can form—of timescale $\tau_1 \approx 3\tau$ following previous observations [35]. Second, the film can deflate before any drops are formed.

The time it takes for the film to fully retract is

$$t_{\rm across} = \frac{R}{V}\left[1 + \frac{\theta_p}{\theta_c}\right]\theta_c, \tag{9}$$

where θ_p is the angle (from the cap's center to) where the film punctures. No film drops can form if $\tau_1/t_{\rm across} = 3\sqrt{6}R^{-5/4}l_c h^{1/4} > 1$. This is determined by assuming $\theta_c = R/(l_c 2\sqrt{3})$ [35] and that the maximum chance of producing drops is when $\theta_p = \theta_c$. The most likely location of puncture was observed to be the foot, but $\theta_p < \theta_c$ for about 35% of the bursts. The equivalent region $h/l_c > (3\sqrt{6})^{-4}(R/l_c)^5$ is shown in Figs. 5(a) and 5(b) without any fitting prefactor, and it marks a boundary between bursting events with and without drops produced. The other mechanism by which no film drops can form is if the cap deflates at a timescale $t_{\rm def}$ faster than τ_1, and an estimate for the deflation time of large bubbles [35] is

$$t_{\rm def} = \left(\frac{6}{7}\right)^{1/3}\frac{R}{V}\left(\frac{\rho_a R}{\rho h}\right)^{1/6}, \tag{10}$$

where ρ_a is the density of the air. No film drops can form if $\tau_1/t_{\rm def}=3\sqrt{7/3}(\rho/\rho_a)^{1/6}R^{-5/12}h^{5/12}>1$, and the equivalent expression $h/l_c > R/l_c(3\sqrt{7/3})^{-12/5}(\rho_a/\rho)^{2/5}$ is shown in Figs. 5(a) and 5(b) also without any fitting prefactor. Both gray regions represent the phase space where drops are not expected to form; $\tau_1 > t_{\rm def}$ and $\tau_1 > t_{\rm across}$, and the data agrees well with these two estimates. The boundaries determined by Eqs. (9) and (10) without any fitting parameters are very robust across all environmental conditions.

It is important to note that while the phase portrait depends only on R and h, multiple variables can affect h as outlined in Sec. V. For example, at $R/l_c \approx 1.5$ in Fig. 5(a), notice that an increase in temperature can increase the film thickness to cross the threshold between producing and not producing drops. Likewise in Fig. 5(b), data of all glycerol % mass values are spread over the entire range and not organized by color.

We note that the phase portrait here is valid for drops that we can detect, i.e., above ≈4 μm in size. The existence of submicron drops outside of the presented phase portrait has been discussed in the literature, see Ref. [36].

VII. NUMBER OF FILM DROPS EJECTED

Assuming that the average drop size is directly proportional to the rim size at the start of the instability as observed [35], $\bar{d} \sim \sqrt{V\tau h} \sim R^{3/8}h^{5/8}$ and that the entire cap volume, $V_{\text{cap}} \sim R^4 h/l_c^2$, is converted into drops leads to a scaling for the average number of drops produced per bursting bubble, $N \sim V_{\text{cap}}/\bar{d}^3$:

$$N = N_0 \left(\frac{R}{l_c}\right)^2 \left(\frac{R}{h}\right)^{7/8}, \tag{11}$$

where N_0 is a dimensionless prefactor.

The number of drops produced for seawater at varied temperatures (in the detected range, i.e., above 4 μm in size) is compared to Eq. (11) in Fig. 6(a) with N_0 found by best-fit to be 0.01 (a range of [0.005, 0.02] describing the spread of the data). Temperature is shown to have only a weak effect on the number production, accounted for the film thickness at burst. The histograms in Figs. 6(b)–6(d) are for $(\frac{R}{l_c})^2(\frac{R}{h})^{7/8}$ ranges of $[10^3, 2\times10^3]$, $[2\times10^3, 4\times10^3]$, and $[4\times10^3, 8\times10^3]$, respectively. For each histogram, the distribution covers almost two full orders of magnitude highlighting the very large statistical variability of the film drop production. Equation (11) captures the general shape of the data, particularly at large values of $(\frac{R}{l_c})^2(\frac{R}{h})^{7/8}$. At small values of $(\frac{R}{l_c})^2(\frac{R}{h})^{7/8}$, the data is overestimated by Eq. (11), because the entire cap is not able to be converted into film drops through one of the two mechanisms described in Sec. VI. Figure 6(a) is log scale, so the bubbles which produce no drops are not shown. The collapse of the data together for all temperatures supports Eq. (11).

The primary effect of the environmental conditions is to alter the average film thickness at burst, $\langle h \rangle$. Like the saltwater data shown in Fig. 6(a), the other datasets show similar agreement with Eq. (11) with prefactors of O(0.01) (a range of [0.005, 0.02] captures the spread). Across all parameters varied in this study, the only information needed to describe the number of drops produced is the capillary length (which does not vary considerably over the range of conditions studied), the thickness of the film when it bursts, and the cap radius.

VIII. CONCLUSION

In this work, bubbles bursting in a wide range of liquid conditions are studied. The lifetime of each bubble is measured to analyze the thin-film cap drainage, and the average thickness of the cap (along with the average lifetime of a bubble) is reported, together with the total number of centrifugal film drops (above about 4 μ in size). We explore the role of changes in liquid viscosity, saltwater temperature, weak surfactant concentration and salinity.

Changes in liquid condition are shown to affect the cap drainage, and a scaling theory proposed in Refs. [9,35] is tested and the prefactors reported. The model which is a function of capillary pressure driving fluid out of the film, viscous drag across the pinched region at the bubble's foot, and marginal regeneration which is a function of Marangoni stress is shown to match the data across all conditions, providing a strong confirmation of the link between film thickness at bursting and lifetime, confirming previous findings [9,35]. The scaling theories, however, do not explain variations in the film thickness at bursting due to changes in salinity, and we report a decrease in

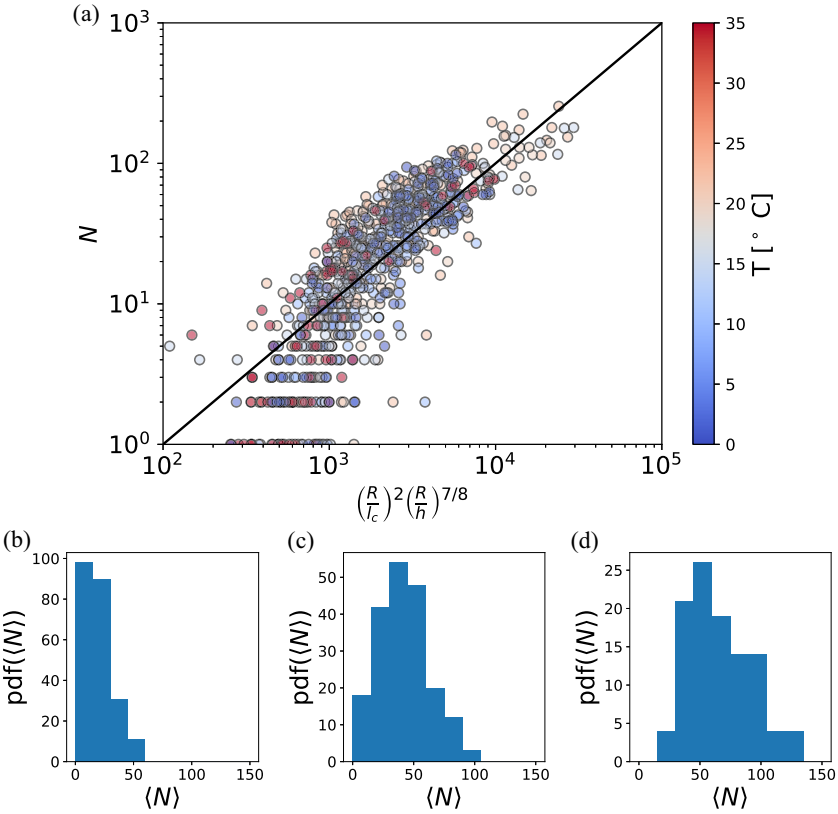

FIG. 6. Number of film drops produced compared to Eq. (11). (a) The number of drops produced in saltwater at various temperatures is compared to Eq. (11) with $N_0 = 0.01$ (a range of [0.005,0.02] describes the spread of the data). The data agrees well with the model for large values of N, while the model over-predicts at lower values because the full liquid volume of the thin-film cap does not become film drops as described in Sec. VI. Histograms of the data are shown in panels (b), (c), and (d) for $(\frac{R}{l_c})^2(\frac{R}{h})^{7/8}$ ranges of $[10^3, 2\times10^3]$, $[2\times10^3, 4\times10^3]$, and $[4\times10^3, 8\times10^3]$, respectively. While the data matches Eq. (11) well, it is still considerably spread (by about two orders of magnitude) across each bin range.

film thickness with decreasing salinity, not explained by existing scaling theories. It is also worth noting that other work [9] observed that saltwater bubbles in ambient conditions lasted longer with thicker films than fresh water bubbles at all lifetimes due to evaporation.

Following the scalings for the thickness at burst from [9,35], we provide prefactors obtained by least square fits to our data as a function of bubble size, and physicochemical variables. The film thickness equation works well across all liquid conditions. However, the average lifetime is widely scattered for all of the datasets, especially for sweeps in temperature in saltwater, suggesting some limitations of the existing scaling theories. The production of film drops is also measured; the bubble's cap radius, the film thickness at burst, and the capillary length fully controls how many drops are produced as predicted by Ref. [35]. The existence of drops is presented, and the theoretical boundaries are shown to be very robust without any fitting parameters across all conditions (again, for drops we are able to measure here, i.e., above 4 microns). Environmental parameters such as temperature are shown to affect the number and existence of drops produced by changing the average film thickness at burst.

Of all properties measured, the lifetime of the bubble is observed to be the most variable, which is consistent with the literature's conflicting conclusions on what effect different environmental

variables have on bubble lifetime; the trends are not well described by the existing models. One area of particular interest is the effect of salt concentration on lifetime and expected film thickness. Our data suggest that changes in salinity impact the film thickness at burst (with saltier water leading to thicker film at burst), such effect not being described by existing models from Refs. [9,35]. These observations join other recent works in the atmospheric science community [58–60] which suggest that water salinity effects submicron drop production.

The results presented here further support the importance of Marangoni effects in film drop production, through film drainage and bursting, as proposed by Refs. [9,35], by providing larger data sets with more systematic variations in physicochemical conditions (surfactant concentration, temperature variations in saltwater, viscosity) while also shedding light on parameters not well understood yet, such as salinity. The accuracy of the scaling laws for various seawater temperature demonstrated here are of particular significance to the atmospheric and ocean science community as the effect of varied ocean conditions on film drop sea spray aerosol is important for global climate modeling [38]. In particular, our individual bubble bursting data suggest that seawater temperature has a weak effect on supermicron droplet number production.

ACKNOWLEDGMENTS

The authors thank the anonymous reviewers for their valuable suggestions. This material is based upon work supported by the National Science Foundation under Grants No. 1849762 and No. 1844932 to L.D. D.B.S. has been partially supported by the National Science Foundation Graduate Research Fellowship Program under Grant No. 1656466 and the High Meadows Environmental Institute at Princeton University through the Mary and Randall Hack '69 Research Fund. The full dataset for every condition presented in this work is available at https://doi.org/10.34770/7q6b-r717.

The authors report no conflict of interest.

APPENDIX A: DATASETS AND LIQUID CONDITIONS

This work studied five different datasets which each varied a single environmental parameter over a sweep of bubble sizes as shown in Table I. The range of the relevant physical parameters as well the number of bubbles recorded in each dataset are shown for each. The physical parameters for synthetic seawater are estimated from Refs. [61,62], and those of the glycerol-water mixtures are estimated from Ref. [63].

TABLE I. This work presents the results from five different datasets which each vary a single liquid parameter: surfactant condition (SDS and Triton X-100), percent glycerol, salinity, and temperature of seawater. The liquid properties at each condition at as well as the number of bubbles are shown. Sea water properties are estimated from Refs. [61,62], and those of the glycerol-water mixtures are estimated from Ref. [63].

	Dataset				
	SDS	Triton X-100	Glycerol	Seawater	Temperature
Primary liquid	DI H_2O	DI H_2O	DI H_2O	DI H_2O	Synthetic weawater
Surfactant: c/μmol	SDS [0, 10, 50, 100, 150]	Triton X-100 [0, 2, 4, 6, 8, 10]	–	–	–
Secondary liquid/% by mass	–	–	Glycerol [0, 10, 20, 30]	Synthetic seawater [0, 50, 100]	–
T/°C	22.5	22.5	22.5	22.5	[1.2, 5, 10, 15, 20, 22.5, 35]
R/mm	2.3–15.0	2.3–15.8	2.3–15.0	2.3–15.9	1.5–15.9
σ/Nm^{-1}	0.070–0.072	0.070–0.072	0.0708–0.072	0.0727–0.0738	0.0713–0.0763
μ/mPa s	0.94	0.94	0.94–2.34	0.94–1.0	0.78–1.9
Number of bubbles	545	852	468	521	903

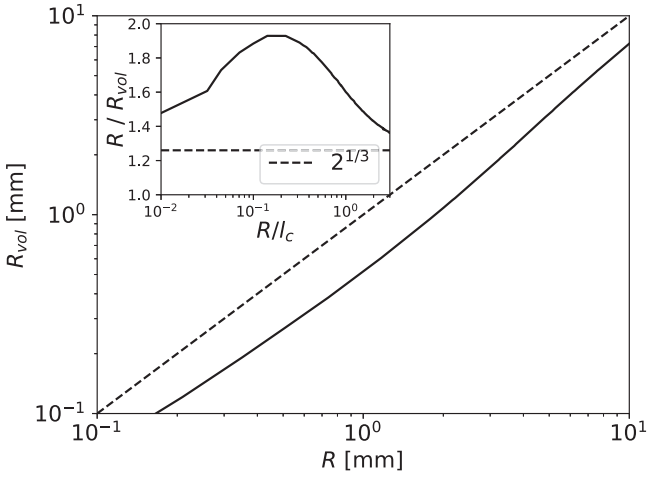

FIG. 7. The main figure shows the relationship between R_{vol} and R. The dashed line indicates where the two quantities would be equal, and as shown $R_{\mathrm{vol}} < R$ for all bubble sizes. The inset shows that the ratio between the two quantities ranges from about $2^{1/3}$ to 2. The dashed line in the inset of $R/R_{\mathrm{vol}} = 2^{1/3}$ is the large bubble ($R \to \infty$) limit where the surface bubble resides completely above the free surface and is a perfect half-sphere.

APPENDIX B: RELATIONSHIP BETWEEN CAP RADIUS AND VOLUMETRIC RADIUS OF SURFACE BUBBLES

The overall size of a surface bubble can be described by multiple metrics. Two of the most commonly used are the cap radius, R, and the volumetric radius, R_{vol} (the radius of a sphere containing the same volume of air). The relationship between these two metrics is shown in Fig. 7, and is determined by solving the Young-Laplace equation for the static shape of a surface bubble. The main figure plots R_{vol} compared to R with the dashed line showing where $R_{\mathrm{vol}} = R$. For all bubble sizes, $R_{\mathrm{vol}} < R$. The ratio of the two metrics is shown in the inset plot. The horizontal dashed line of the inset $R/R_{\mathrm{vol}} = 2^{1/3}$ shows the large bubble ($R \to \infty$) limit where the surface bubble resides completely above the free surface and is a half-sphere.

[1] E. R. Lewis and S. E. Schwartz, in *Sea Salt Aerosol Production: Mechanisms, Methods, Measurements, and Models*, edited by C. J. Hawkesworth, K. E. Karlstrom, and R. S. J. Sparks, Geophysical Monograph Series (Wiley, New York, NY, 2004).

[2] K. A. Prather, T. H. Bertram, V. H. Grassian, G. B. Deane, M. D. Stokes, P. J. DeMott, L. I. Aluwihare, B. P. Palenik, F. Azam, J. H. Seinfeld, R. C. Moffet, M. J. Molina, C. D. Cappa, F. M. Geiger, G. C. Roberts, L. M. Russell, A. P. Ault, J. Baltrusaitis, D. B. Collins, C. E. Corrigan, L. A. Cuadra-Rodriguez, C. J. Ebben, S. D. Forestieri, T. L. Guasco, S. P. Hersey, M. J. Kim, W. F. Lambert, R. L. Modini, W. Mui, B. E. Pedler, M. J. Ruppel, O. S. Ryder, N. G. Schoepp, R. C. Sullivan, and D. Zhao, Bringing the ocean into the laboratory to probe the chemical complexity of sea spray aerosol, Proc. Natl. Acad. Sci. USA **110**, 7550 (2013).

[3] L. Deike, Mass transfer at the ocean–atmosphere interface: the role of wave breaking, droplets, and bubbles, Annu. Rev. Fluid Mech. **54**, 191 (2022).

[4] F. Veron, Ocean spray, Annu. Rev. Fluid Mech. **47**, 507 (2015).

[5] G. de Leeuw, E. L. Andreas, M. D. Anguelova, C. W. Fairall, E. R. Lewis, C. O'Dowd, M. Schulz, and S. E. Schwartz, Production flux of sea spray aerosol, Rev. Geophys. **49**, 2010RG000349 (2011).

[6] F. Paulot, D. Paynter, M. Winton, P. Ginoux, M. Zhao, and L. W. Horowitz, Revisiting the impact of sea salt on climate sensitivity, Geophys. Res. Lett. **47**, e2019GL085601 (2020).
[7] K. Sampath, N. Afshar-Mohajer, L. D. Chandrala, W. S. Heo, J. Gilbert, D. Austin, K. Koehler, and J. Katz, Aerosolization of crude oil-dispersant slicks due to bubble bursting, J. Geophys. Res.: Atmos. **124**, 5555 (2019).
[8] A. H. Woodcock, Note concerning human respiratory irritation associated with high concentrations of plankton and mass mortality of marine organisms, J. Mar. Res. **7**, 56 (1948).
[9] S. Poulain, E. Villermaux, and L. Bourouiba, Ageing and burst of surface bubbles, J. Fluid Mech. **851**, 636 (2018).
[10] D. Johnson, R. Lynch, C. Marshall, K. Mead, and D. Hirst, Aerosol generation by modern flush toilets, Aerosol Sci. Technol. **47**, 1047 (2013).
[11] S. Poulain and L. Bourouiba, Disease transmission via drops and bubbles, Phys. Today **72**, 70 (2019).
[12] P. Vega-Martínez, O. R. Enríquez, and J. Rodríguez-Rodríguez, Some topics on the physics of bubble dynamics in beer, Beverages **3**, 38 (2017).
[13] E. Ghabache, G. Liger-Belair, A. Antkowiak, and T. Séon, Evaporation of droplets in a Champagne wine aerosol, Sci. Rep. **6**, 25148 (2016).
[14] M. Manga and H. A. Stone, Interactions between bubbles in magmas and lavas: Effects of bubble deformation, J. Volcanol. Geotherm. Res. **63**, 267 (1994).
[15] E. Villermaux, X. Wang, and L. Deike, Bubbles spray aerosols: Certitudes and mysteries, PNAS Nexus **1**, pgac261 (2022).
[16] J. J. Bikerman, Persistence of bubbles on inorganic salt solutions, J. Appl. Chem. **18**, 266 (1968).
[17] M. D. Anguelova and P. Huq, Effects of salinity on surface lifetime of large individual bubbles, J. Mar. Sci. Eng. **6**, 1 (2017).
[18] S. Liu, C. C. Liu, K. D. Froyd, G. P. Schill, D. M. Murphy, T. P. Bui, J. M. Dean-Day, B. Weinzierl, M. Dollner, G. S. Diskin, G. Chen, and R. S. Gao, Sea spray aerosol concentration modulated by sea surface temperature, Proc. Natl. Acad. Sci. USA **118**, e2020583118 (2021).
[19] S. D. Forestieri, K. A. Moore, R. Martinez Borrero, A. Wang, M. D. Stokes, and C. D. Cappa, Temperature and composition dependence of sea spray aerosol production, Geophys. Res. Lett. **45**, 7218 (2018).
[20] H. Grythe, J. Ström, R. Krejci, P. Quinn, and A. Stohl, A review of sea-spray aerosol source functions using a large global set of sea salt aerosol concentration measurements, Atmos. Chem. Phys. **14**, 1277 (2014).
[21] L. Jaeglé, P. K. Quinn, T. S. Bates, B. Alexander, and J. T. Lin, Global distribution of sea salt aerosols: New constraints from *in situ* and remote sensing observations, Atmos. Chem. Phys. **11**, 3137 (2011).
[22] J. Ovadnevaite, A. Manders, G. De Leeuw, D. Ceburnis, C. Monahan, A. I. Partanen, H. Korhonen, and C. D. O'Dowd, A sea spray aerosol flux parameterization encapsulating wave state, Atmos. Chem. Phys. **14**, 1837 (2014).
[23] J. Zábori, R. Krejci, A. M. Ekman, E. M. Märtensson, J. Ström, G. De Leeuw, and E. D. Nilsson, Wintertime Arctic Ocean sea water properties and primary marine aerosol concentrations, Atmos. Chem. Phys. **12**, 10405 (2012).
[24] J. Zábori, M. Matisans, R. Krejci, E. D. Nilsson, and J. Ström, Artificial primary marine aerosol production: A laboratory study with varying water temperature, salinity, and succinic acid concentration, Atmos. Chem. Phys. **12**, 10709 (2012).
[25] M. E. Salter, E. D. Nilsson, A. Butcher, and M. Bilde, On the seawater temperature dependence of the sea spray aerosol generated by a continuous plunging jet, J. Geophys. Res.: Atmos. **119**, 9052 (2014).
[26] A. M. Worthington, *A Study of Splashes*, Nineteenth Century Collections Online: Photography: The World through the Lens (Longmans, Green, and Company, London, UK, 1908).
[27] E. Ghabache, A. Antkowiak, C. Josserand, and T. Séon, On the physics of fizziness: How bubble bursting controls droplets ejection, Phys. Fluids **26**, 121701 (2014).
[28] J. M. Gordillo and J. Rodríguez-Rodríguez, Capillary waves control the ejection of bubble bursting jets, J. Fluid Mech. **867**, 556 (2019).
[29] P. L. Walls, L. Henaux, and J. C. Bird, Jet drops from bursting bubbles: How gravity and viscosity couple to inhibit droplet production, Phys. Rev. E **92**, 021002 (2015).

[30] L. Deike, E. Ghabache, G. Liger-Belair, A. K. Das, S. Zaleski, S. Popinet, and T. Séon, Dynamics of jets produced by bursting bubbles, Phys. Rev. Fluids **3**, 013603 (2018).
[31] R. Mead-Hunter, M. M. Gumulya, A. J. King, and B. J. Mullins, Ejection of droplets from a bursting bubble on a free liquid surface—A dimensionless criterion for "jet" droplets, Langmuir **34**, 6307 (2018).
[32] D. C. Blanchard, The size and height to which jet drops are ejected from bursting bubbles in seawater, J. Geophys. Res. **94**, 10999 (1989).
[33] S.-C. Georgescu, J.-L. Achard, and E. Canot, Jets drops ejection in bursting gas bubble process, J. Mec. Theor. Appl. **21**, 265 (2020).
[34] A. Berny, S. Popinet, T. Séon, and L. Deike, Statistics of jet drop production, Geophys. Res. Lett. **48**, e2021GL092919 (2021).
[35] H. Lhuissier and E. Villermaux, Bursting bubble aerosols, J. Fluid Mech. **696**, 5 (2012).
[36] X. Jiang, L. Rotily, E. Villermaux, and X. Wang, Submicron drops from flapping bursting bubbles, Proc. Natl. Acad. Sci. USA **119**, e2112924119 (2021).
[37] X. Wang, G. B. Deane, K. A. Moore, O. S. Ryder, M. D. Stokes, C. M. Beall, D. B. Collins, M. V. Santander, S. M. Burrows, C. M. Sultana, and K. A. Prather, The role of jet and film drops in controlling the mixing state of submicron sea spray aerosol particles, Proc. Natl. Acad. Sci. USA **114**, 6978 (2017).
[38] L. Deike, B. G. Reichl, and F. Paulot, A mechanistic sea spray generation function based on the sea state and the physics of bubble bursting, AGU Adv. **3**, e2022AV000750 (2022).
[39] B. Néel and L. Deike, Collective bursting of free-surface bubbles, and the role of surface contamination, J. Fluid Mech. **917**, A46 (2021).
[40] Y. Toba, Drop production by bursting of air bubbles on the sea surface (II) theoretical study on the shape of floating bubbles, J. Oceanogr. Soc. Jpn. **15**, 121 (1959).
[41] H. M. Princen, Shape of a fluid drop at a liquid-liquid interface, J. Colloid Sci. **18**, 178 (1963).
[42] A. Berny, L. Deike, T. Séon, and S. Popinet, Role of all jet drops in mass transfer from bursting bubbles, Phys. Rev. Fluids **5**, 033605 (2020).
[43] L. Champougny, M. Roché, W. Drenckhan, and E. Rio, Life and death of not so "bare" bubbles, Soft Matter **12**, 5276 (2016).
[44] K. Danov, D. S. Valkovska, and I. B. Ivanov, Effect of surfactants on the film drainage, J. Colloid Interface Sci. **211**, 291 (1999).
[45] D. Langevin, On the rupture of thin films made from aqueous surfactant solutions, Adv. Colloid Interface Sci. **275**, 102075 (2020).
[46] V. A. Nierstrasz and G. Frens, Marginal regeneration and the Marangoni effect, J. Colloid Interface Sci. **215**, 28 (1999).
[47] G. Debrégeas, P. G. De Gennes, and F. Brochard-Wyart, The life and death of "bare" viscous bubbles, Science **279**, 1704 (1998).
[48] C. Bartlett, A. T. Oratis, M. Santin, and J. C. Bird, Universal non-monotonic drainage in large bare viscous bubbles, Nat. Commun. **14**, 877 (2023).
[49] V. A. Nierstrasz and G. Frens, Marginal regeneration in thin vertical liquid films, J. Colloid Interface Sci. **207**, 209 (1998).
[50] J. Miguet, F. Rouyer, and E. Rio, The life of a surface bubble, Molecules **26**, 1317 (2021).
[51] S. Poulain and L. Bourouiba, Biosurfactants change the thinning of contaminated bubbles at bacteria-laden water interfaces, Phys. Rev. Lett. **121**, 204502 (2018).
[52] P. D. Howell and H. A. Stone, On the absence of marginal pinching in thin free films, Eur. J. Appl. Math. **16**, 569 (2005).
[53] K. J. Mysels, K. Shinoda, and S. Frankel, *Soap Films, Studies of Their Thinning and a Bibliography* (Pergamon Press, New York, NY, 1959).
[54] A. Gros, A. Bussonniere, S. Nath, and I. Cantat, Marginal regeneration in a horizontal film: Instability growth law in the nonlinear regime, Phys. Rev. Fluids **6**, 024004 (2021).
[55] Y. Couder, J. Chomaz, and M. Rabaud, On the hydrodynamics of soap films, Physica D **37**, 384 (1989).
[56] J. Miguet, M. Pasquet, F. Rouyer, Y. Fang, and E. Rio, Marginal regeneration-induced drainage of surface bubbles, Phys. Rev. Fluids **6**, L101601 (2021).

[57] J. Seiwert, R. Kervil, S. Nou, and I. Cantat, Velocity field in a vertical foam film, Phys. Rev. Lett. **118**, 048001 (2017).

[58] S. Christiansen, M. E. Salter, E. Gorokhova, Q. T. Nguyen, and M. Bilde, Sea spray aerosol formation: Laboratory results on the role of air entrainment, water temperature, and phytoplankton biomass, Environ. Sci. Technol. **53**, 13107 (2019).

[59] J. Zinke, E. D. Nilsson, P. Zieger, and M. E. Salter, The effect of seawater salinity and seawater temperature on sea salt aerosol production, J. Geophys. Res.: Atmos. **127**, e2021JD036005 (2022).

[60] L. Dubitsky, M. D. Stokes, G. B. Deane, and J. C. Bird, Effects of salinity beyond coalescence on submicron aerosol distributions, J. Geophys. Res.: Atmos. **128**, e2022JD038222 (2023).

[61] M. H. Sharqawy, J. H. Lienhard V, and S. M. Zubair, Thermophysical properties of seawater: A review of existing correlations and data, Desalin. Water Treat. **16**, 354 (2010).

[62] K. G. Nayar, M. H. Sharqawy, L. D. Banchik, and J. H. Lienhard, Thermophysical properties of seawater: A review and new correlations that include pressure dependence, Desalination **390**, 1 (2016).

[63] S. R. Gregory, Physical properties of glycerine, in *Glycerine* (CRC Press, Boca Raton, FL, 1991), pp. 113–156.